Improved Winter European Atmospheric Blocking Frequencies in High-Resolution Global Climate Simulations

AGU PUBLICATIONS

Journal of Advances in Modeling Earth Systems

RESEARCH ARTICLE

10.1002/2017MS001082

Improved Winter European Atmospheric Blocking Frequencies in High-Resolution Global Climate Simulations

P. Davini[1,2], S. Corti[3], F. D'Andrea[1], G. Rivière[1], and J. von Hardenberg[2]

[1]Laboratoire de Météorologie Dynamique/IPSL, École Normale Supérieure, PSL Research University, CNRS, Paris, France, [2]Istituto di Scienze dell'Atmosfera e del Clima, Consiglio Nazionale delle Ricerche (ISAC-CNR), Torino, Italy, [3]Istituto di Scienze dell'Atmosfera e del Clima, Consiglio Nazionale delle Ricerche (ISAC-CNR), Bologna, Italy

Key Points:
- 25-km resolution EC-Earth GCM is able to simulate winter atmospheric blocking frequency over Europe with a negligible bias
- Improvements are caused by the more refined orography and by the weakening of the storm track
- Blocking duration and jet speed are underestimated suggesting that positive results are due to bias compensation

Correspondence to:
P. Davini,
pdavini@lmd.ens.fr

Citation:
Davini, P., Corti, S., D'Andrea, F., Rivière, G., & von Hardenberg, J. (2017). Improved Winter European Atmospheric Blocking Frequencies in High-Resolution Global Climate Simulations. *Journal of Advances in Modeling Earth Systems*, *9*, 2615–2634. https://doi.org/10.1002/2017MS001082.

Received 7 JUN 2017
Accepted 7 OCT 2017
Accepted article online 16 OCT 2017
Published online 17 NOV 2017

Abstract The numerical simulation of atmospheric blocking, in particular over the Euro-Atlantic region, still represents a main concern for the climate modeling community. We discuss the Northern Hemisphere winter atmospheric blocking representation in a set of 30 year atmosphere-only simulations using the EC-Earth Earth System Model with several ensemble members at five different horizontal resolutions (from 125 to 16 km). Results show that the negative bias in blocking frequency over Europe becomes negligible at resolutions of about 40 and 25 km. A combined effect by the more resolved orography and by a change in tropical precipitation is identified as the source of an upper tropospheric planetary wave. At the same time, a weakening of the meridional temperature gradient reduces the upper level baroclinicity and the zonal mean winds. Following these changes, in the high-resolution configurations the Atlantic eddy-driven jet stream is weakened favoring the breaking of synoptic Rossby waves over the Atlantic ridge and thus increasing the simulated European blocking frequency. However, at high-resolution the Atlantic jet stream is too weak and the blocking duration is still underestimated. This suggests that the optimal blocking frequencies are achieved through compensation of errors between eddies found at upper levels (too strong) and eddies at lower levels (too weak). This also implies that eddies are not necessarily better represented at higher resolutions.

1. Introduction

Atmospheric blocking is a midlatitude weather pattern characterized by a quasi-stationary, long-lasting, equivalent-barotropic, high-pressure system that "blocks" and diverts the movement of the synoptic cyclones (Berggren et al., 1949; Rex, 1950). It usually occurs following the breaking of a Rossby wave in diffluence regions at the exit of the Pacific and Atlantic storm track. Here a subtropical low-vorticity air mass is advected poleward, developing an anticyclonic circulation (Davini et al., 2012; Pelly & Hoskins, 2003; Tyrlis & Hoskins, 2008a). Blocking occurs more frequently in winter and spring—when the jet streams and the storm tracks are stronger—although it may be observed all over the year (Barriopedro et al., 2006; Tyrlis & Hoskins, 2008b).

Atmospheric blocking is characterized by a complex dynamic, and often by a blurry definition: several complementary phenomena operate within the word "blocking," from Rossby wave breaking (Masato et al., 2011; Pelly & Hoskins, 2003) to transient baroclinic eddies (Green, 1977; Nakamura et al., 1997; Shutts, 1983), passing through diabatic effects (Pfahl et al., 2015) and the resonance with planetary waves (Austin, 1980). Even if all these mechanisms contribute to the onset and maintenance of blocking anomalies, to this day a comprehensive theoretical interpretation of blocking dynamics has yet to be developed: this is mainly due to its nonlinear dynamics, which makes theoretical approaches often ineffective in the real world (Charney & DeVore, 1979; Malguzzi & Malanotte-Rizzoli, 1984; McWilliams, 1980). Moreover, finding a common objective detection index is also not straightforward: several indices have been developed (see Barriopedro et al., 2010, for details), both monodimensional and bidimensional, using absolute fields or anomalies, potential vorticity or geopotential height, sometimes leading to contradicting results (Barnes et al., 2014; Scherrer et al., 2006). However, they all concur in defining a "blocking frequency," i.e., the percentage of number of days for which blocking is occurring at a certain grid point.

Among others, one of the reasons why blocking is still in the spotlight of climate research after more than 60 years is that numerical models have always shown limited skill in reproducing it, in particular over the

Euro-Atlantic sector. This poor skill is still widely documented for general circulation models, both for weather prediction (Matsueda, 2011; Tibaldi & Molteni, 1990) and for climate purposes (Davini & D'Andrea, 2016; Vial & Osborn, 2012). Even the more recent analyses from the Coupled Model Intercomparison Project-Phase 5 (Taylor et al., 2012) still show a negative bias in blocking frequencies, especially over Europe (Anstey et al., 2013; Dunn-Sigouin and Son, 2013; Masato et al., 2013)

The origin of the underestimation of blocking frequencies over Europe has been often connected with an incorrect representation of the mean state that affects Rossby waves propagation and consequently blocking dynamics (Scaife et al., 2010; Vial & Osborn, 2012). In general, it has been shown that a large part of the blocking bias is associated with the mean state bias rather than to the capacity of representing single blocking events (Davini & D'Andrea, 2016).

A good representation of sea-surface temperatures (SST) has been claimed to be important, showing that simulations can be improved by reducing biases in the North Atlantic SSTs (O'Reilly et al., 2016; Scaife et al., 2011). However, this can be considerably model-dependent (Davini & D'Andrea, 2016).

Finally, an increase in the horizontal resolution of the atmospheric model has generally been invoked as a solution to improve blocking (Jung et al., 2012; Matsueda et al., 2009): again, even if this clearly emerges in multimodel assessment of climate models (Davini & D'Andrea, 2016), there is evidence that it may be ineffective for some specific models (Schiemann et al., 2017).

Blocking may benefit of horizontal grid refinement for at least two main reasons: first, this is associated with better resolved transient eddy fluxes, which should sustain the blocking persistence (Shutts, 1983). Second, higher horizontal resolution implies a better resolved mean orography, that can affect the mean state by shaping the planetary waves (Berckmans et al., 2013; Jung et al., 2012). It is important to recall that orography-related improvements can be obtained also with the introduction/improvement of parameterizations that mimic the drag on the flow by subgrid orography (Jung et al., 2010a; Pithan et al., 2016). These improvements can affect both the model variability and the model mean state: for instance, a finer grid can provide an improvement in the jet stream properties, which in turn modifies the Rossby wave guide and indirectly help the blocking dynamics.

Recently Davini et al. (2017) presented preliminary results of the Climate SPHINX (Stochastic Physics HIgh resolutioN eXperiments) PRACE project, a set of ensemble simulations aimed at evaluating the sensitivity of present and future climate to model resolution and stochastic parameterization, with resolutions from 125 to 16km. They showed that increased atmospheric horizontal resolution can provide a significant benefit for the simulation of European blocking, as illustrated by a basic monodimensional blocking index.

In this work we aim at extending the results of Davini et al. (2017), by analyzing the output of present day climate simulations performed within the SPHINX project. In particular, we use a modern bidimensional blocking index comparing EC-Earth to other CMIP5 models, in order to accurately assess whether or not the improvements seen can be associated with resolution increase. Further, we investigate which are the reasons behind these changes.

2. Data and Methods

A subset of the simulations carried out within the Climate SPHINX project (Davini et al., 2017) is used. This is made by an ensemble of atmospheric-only simulations for 30 consecutive years, from 1979 up to 2008, with forcing according to the historical CMIP5 protocol (Moss et al., 2010). The runs were performed with version 3.1 of the atmosphere-ocean Earth System Model EC-Earth (Hazeleger et al., 2010, 2012).

The atmospheric component of EC-Earth is based on cycle 36r4 of the Integrated Forecast System (IFS) circulation model (ECWMF, 2010), which has been developed by the European Centre for Medium Range Weather Forecasts (ECMWF). The model has been tuned and improved for climate purposes by the EC-Earth Consortium. To represent land surface dynamics, IFS integrates the Hydrology Tiled ECMWF Scheme of Surface Exchanges over Land (H-TESSEL) land surface scheme (Balsamo et al., 2009). A specific feature of the Climate SPHINX simulations is to have the same vertical grid with 91 levels (L91) but to explore five different horizontal resolutions with several ensemble members: 10 ensemble members are run at T159 (∼125km), 10 at T255 (∼80 km), six at T511 (∼40 km), three at T799 (∼25 km), and one at T1279 (∼16 km).

SST and sea ice concentration for the Climate SPHINX simulations have been obtained from the HadISST2.1.1 data set (Titchner & Rayner, 2014). It is important to point out that model tuning has been performed only for the "standard" T255 EC-Earth configuration, i.e., the one that will be used for the upcoming CMIP6 project. Therefore energy budgets at resolutions different from T255 present small biases that, together with details on the setup of the Climate SPHINX simulations, are described in Davini et al. (2017).

In order to provide a comparison with other state-of-the-art Global Climate Models (GCMs), 18 different atmospheric-only climate models from the CMIP5 project have been considered. A single ensemble member over the same time window (1979–2008) has been analyzed for ACCESS1-0, BCC-CSM1-1, BNU-ESM, CanAM4, CCSM4, CNRM-CM5, EC-Earth, FGOALS-g2, GFDL-CM3, HadGEM2-A, IPSL-CM5A-LR, IPSL-CM5A-MR, IPSL-CM5B-LR, MIROC5, MPI-ESM-LR, MPI-ESM-MR, MRI-CGCM3, and NorESM1-M. For convenience, since these are atmospheric-only models, we will refer to them as AMIP5 in the following.

In order to evaluate biases of the EC-Earth simulations, we use 1979–2008 data from the ECMWF ERA-Interim Reanalysis (Dee et al., 2011) and, for blocking diagnostic only, also from the NCEP/NCAR Reanalysis (Kalnay et al., 1996). In all the manuscript we focus on the extended winter season (defined as December–March, DJFM), for a total of 29 consecutive seasons. Before any computation, all data are interpolated on a common 2.5° x 2.5° grid with a second-order conservative remapping method.

To objectively recognize blocking events a 2-D index based on the reversal of the gradient of geopotential height measured at 500hPa (Z500) has been adopted (Davini et al., 2012; Scherrer et al., 2006). This is an extension of the most known index by Tibaldi and Molteni (1990). Two meridional gradients of geopotential height are defined:

$$GHGS(\lambda_0,\phi_0)=\frac{Z500(\lambda_0,\phi_0)-Z500(\lambda_0,\phi_S)}{\phi_0-\phi_S}, \tag{1}$$

$$GHGN(\lambda_0,\phi_0)=\frac{Z500(\lambda_0,\phi_N)-Z500(\lambda_0,\phi_0)}{\phi_N-\phi_0} \tag{2}$$

and ϕ_0 ranges from 30°N to 75°N while λ_0 ranges from 0° to 360°. $\phi_S = \phi_0 - 15°$, $\phi_N = \phi_0 + 15°$. Instantaneous Blocking is thus identified when:

$$GHGS(\lambda_0,\phi_0) > 0 \qquad GHGN(\lambda_0,\phi_0) < -10\mathrm{m}/^{\circ}\,\mathrm{lat} \tag{3}$$

Further constraints have been applied to Instantaneous Blocking. First, Large-Scale Blocking is defined when an Instantaneous Blocking is extended for at least 15° of continuous longitude. Second, a Large-Scale Blocking Event is defined for each grid point when a Large-Scale Blocking is occurring within 5° lon (2 grid points) and 2.5° lat (1 grid point) of it. Finally, a Blocking Event at a certain grid point is defined when a Large-Scale Blocking Events lasts for at least 5 days. Those constraints ensure that Blocking Events have a significant longitudinal extension, are persistent and quasi-stationary. The percentage of days per season in which Blocked Events occur (i.e., blocked days) defines the blocking frequency climatology. A complete description of the blocking climatology and of the blocking detection scheme may be found in Davini et al. (2012).

We make use of other diagnostics to study the midlatitude climate variability. In order to evaluate the baroclinic instability changes along the storm track, we make use the Eady Growth Rate maximum, defined following Vallis (2006):

$$\sigma_{BI}=0.3068\ f\left|\frac{\partial\bar{u}}{\partial z}\right|N^{-1}, \tag{4}$$

where the overbar denotes a time average, u is the eastward wind component, f the Coriolis frequency, and N is the Brunt-Väisälä frequency, defined as:

$$N^2=\frac{g}{\theta}\frac{\partial\bar{\theta}}{\partial z}, \tag{5}$$

where θ is the air potential temperature and g the standard gravity acceleration.

High-frequency variability is measured applying a bandpass Fourier filtering between 2 and 6 days and filtered variables are hereafter indicated with a prime sign. Transient eddies activity is then evaluated using the standard deviation of the bandpass filtered daily geopotential height (Z'). In analogy, eddy kinetic energy (EKE) is computed using the bandpass filtered zonal and meridional wind so that $EKE = 1/2(u'^2 + v'^2)$. In addition, the low level heat fluxes are evaluated to provide supplementary information on the storm track development. These are measured as the product of the bandpass filtered meridional velocity and temperature so that $HF = v'T'$.

Two more diagnostics are introduced to evaluate the transfer of energy from the mean flow to the eddies and vice versa. The role of the eddy forcing on the large-scale flow is analyzed using the scalar product $\boldsymbol{E} \cdot \boldsymbol{D}$, which is a measure of barotropic exchange of kinetic energy between the transient eddies and the large-scale flow (Cai & Mak, 1990). $\boldsymbol{E}$ is defined as the horizontal part of the local Eliassen-Palm vector (Trenberth, 1986) which is very similar to the Hoskins $\boldsymbol{E}$-vector (Hoskins et al., 1983) and is computed evaluating the bandpass filtered (2–6 days) u and v as

$$\boldsymbol{E} = \left(\frac{v'^2 - u'^2}{2}, -u'v' \right). \tag{6}$$

Conversely, $\boldsymbol{D}$ is the deformation of the mean field, where D_x is the stretching deformation and D_y the shear deformation (Black & Dole, 2000; Cai & Mak, 1990):

$$\boldsymbol{D} = \left(\frac{\partial \bar{u}}{\partial x} - \frac{\partial \bar{v}}{\partial y}, \frac{\partial \bar{v}}{\partial x} + \frac{\partial \bar{u}}{\partial y} \right). \tag{7}$$

$\boldsymbol{E} \cdot \boldsymbol{D}$ is usually computed in the upper troposphere (i.e., 250 hPa) where it reaches its highest values. Positive values of the $\boldsymbol{E} \cdot \boldsymbol{D}$ scalar (also known as barotropic energy conversion) indicate regions where the mean flow is feeding the synoptic eddies, while negative values point to regions where the mean flow is fed by the eddies. Large negative values are commonly seen in the exit region of the storm track, where the eddies are "barotropizing" the flow while smaller positive values are found in the entrance region (Black & Dole, 2000; Lee, 2000).

Similarly to the barotropic conversion, we introduce the baroclinic conversion energy term. It is defined following Riviere and Joly (2006) as

$$F = -\frac{1}{S} v'\theta' \frac{\partial \bar{\theta}}{\partial y}, \tag{8}$$

which is the product between the meridional temperature gradient and the high-frequency heat fluxes divided by a static stability parameter S, here defined as

$$S = -\frac{R}{p_0} \left(\frac{p_0}{p} \right)^{\frac{c_v}{c_p}} \frac{\partial \bar{\theta}}{\partial p}, \tag{9}$$

where p_0 is the reference density (i.e., 1000 hPa), c_v and c_p are the atmospheric specific heat at constant volume and pressure, respectively, and R is the gas constant for dry air. The baroclinic conversion term F, usually evaluated in lower-middle troposphere, is mainly characterized by positive values, highlighting areas where the available potential energy of the mean flow is transferred to the eddies, namely in the core of the storm tracks (Cai & Mak, 1990; Riviere & Joly, 2006).

3. Results

3.1. Blocking Frequency

The top row of Figure 1 shows the climatology of blocking events frequency averaged over the extended winter season (December–March, DJFM) for the 1979–2008 period. The ensemble mean of the five resolutions explored in Climate SPHINX is plotted.

In Figure 1 two main areas of blocking are identified, over the Pacific and the Atlantic basins. The maximum blocking events frequency is found over the Pacific at high latitudes. Conversely over the Atlantic sector a first relative maximum is seen over Greenland—which is associated with cyclonic Rossby wave breaking—

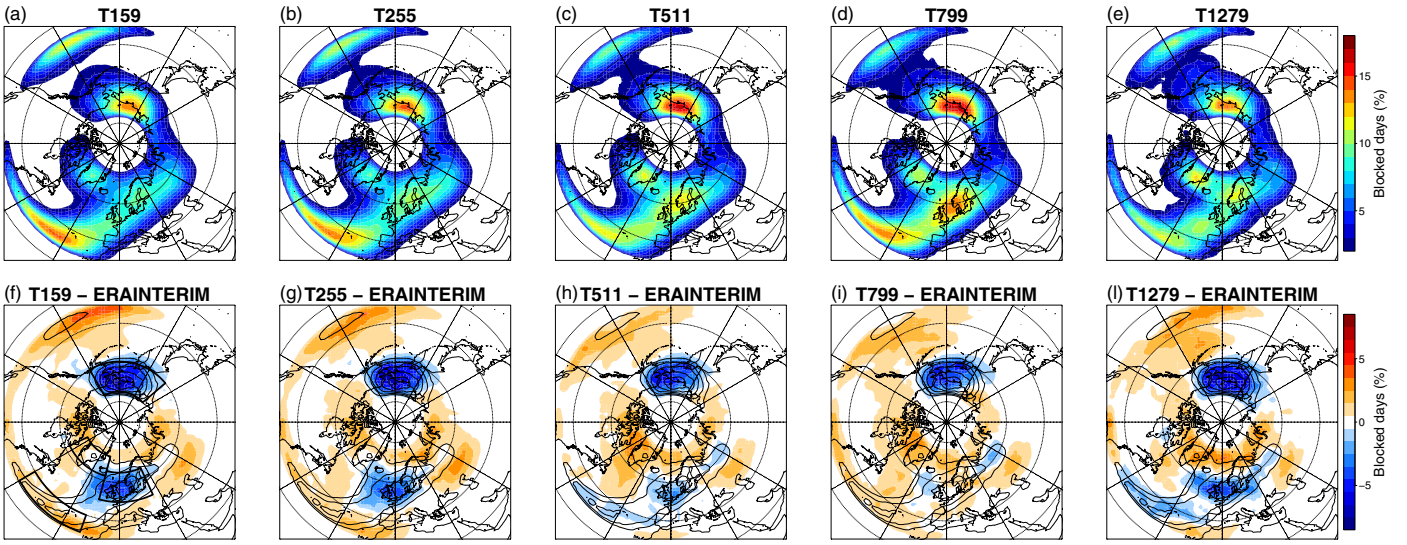

Figure 1. (a–e) DJFM 1979–2008 blocking events (blocked days) for the EC-Earth ensemble mean at five different resolution. (f–l) EC-Earth model biases (colors) against ERA Interim reanalysis (contours). Contours are drawn every 3%. Boxes identifying the different regions used in Figure 3 are shown in Figure 1f.

and a second one over Europe—which is defining the well-known European blocking (Masato et al., 2011). In both basins over the low latitudes relative maxima of blocking frequencies are found, mainly associated with anticyclonic Rossby wave breaking (Davini et al., 2012).

Even at the lowest resolution (T159, ∼125 km, Figure 1f), when compared to recent CMIP5 models (e.g., Anstey et al., 2013, which used a similar index), EC-Earth shows a limited bias. However the well-known GCM bias characterized by an underestimation of blocking over Central Europe and by an overestimation at lower latitude is clearly visible. In addition, EC-Earth presents a considerable negative bias over the North Pacific.

The improvement provided by the grid refinement is evident over the Euro-Atlantic region. In this area, the bias decreases monotonically as resolution is increased up to T799. In this latter configuration (i.e., T799, ∼25 km), the blocking bias is actually negligible over most of the Euro-Atlantic sector (Figure 1i). On the other hand, over the Pacific region the negative bias—albeit reduced—is still evident even at higher resolutions.

In apparent contradiction with the general improvement of the blocking climatology with the increase of resolution, a nonnegligible deterioration of the blocking climatology is observed for the T1279 configuration. Such unexpected failure in the model performance will be discussed in the following sections. However, it is worth to highlight that only one ensemble member is available for this configuration, therefore the resulting climatological blocking events frequency can be affected by the subsampling of natural variability.

A common tool to summarize the performance of climate models is the Taylor diagram (Taylor, 2001). A Taylor diagram provides a compact measure of different pattern-based statistics comparing a model field f to a reference field r (usually a reanalysis data set). It includes in the same plot information on the spatial correlation R (i.e., the Pearson correlation coefficient), on the ratio of the pattern standard deviations σ_f/σ_r and on the root mean square error E evaluated against the reference field. Each model is represented as a dot on a polar plot in the correlation/variance space where $E=\sigma_f^2+\sigma_r^2-2\sigma_r\sigma_f R$. Statistics are computed introducing an equal-area weighting based on the cosine of the latitude. The ERA-Interim reanalysis is defined as reference field and only grid points for which ERA-Interim blocking events frequencies are not zero are considered.

Figure 2 shows the Taylor diagram for the DJFM blocking climatology for each ensemble member (using different colors for each resolution) and for the 18 atmosphere-only AMIP5 models considered in this work (in grey). The reference field, i.e., ERA-Interim Reanalysis, is found at (1,0) and it is highlighted by a black

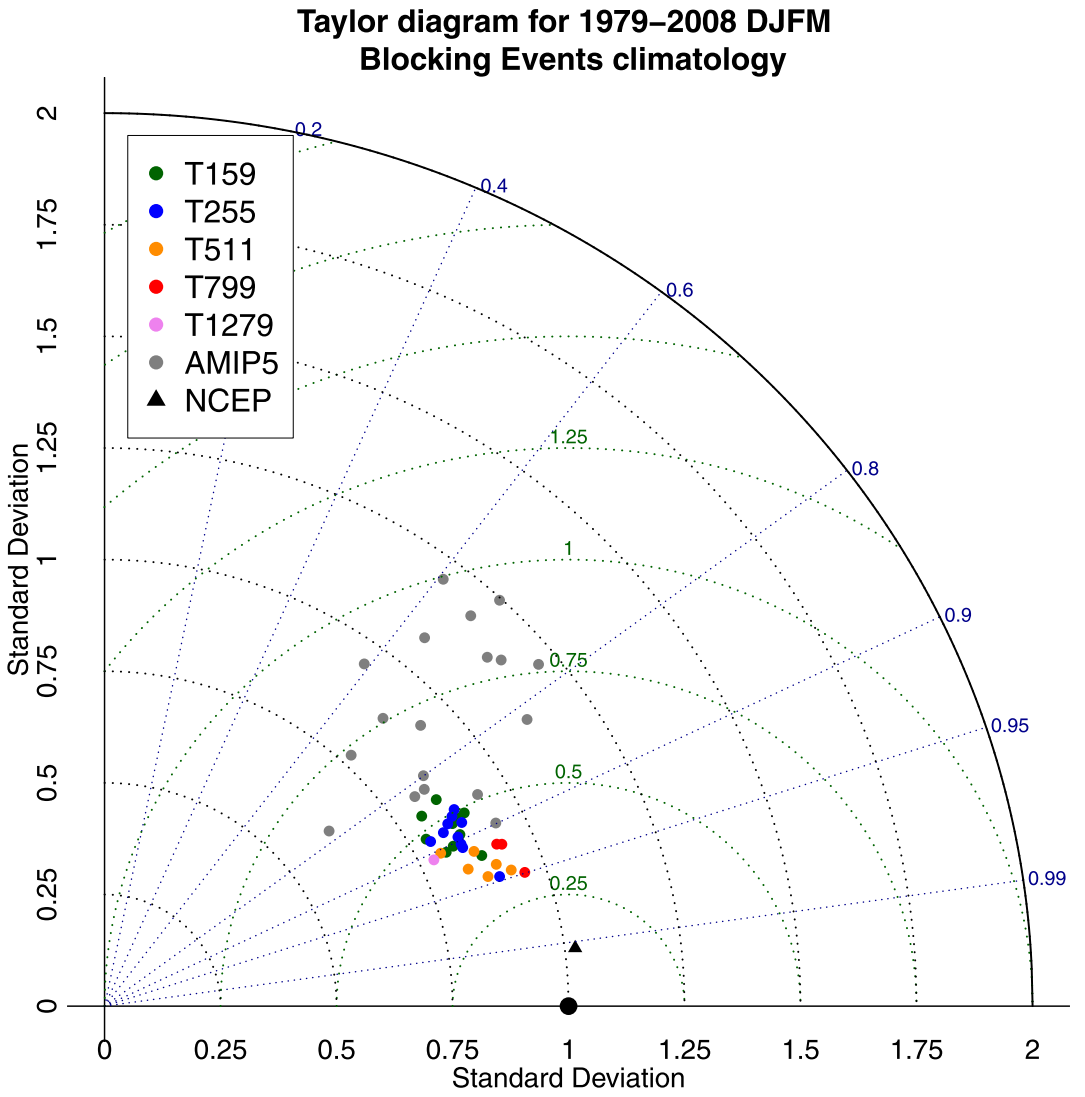

Figure 2. Taylor diagram for the blocking events frequency climatological patterns, showing each ensemble member (colors), each AMIP5 model (grey) and NCEP/NCAR (black triangle). The reference field is given by ERA-Interim (black dot). Blue lines show the correlation coefficients *R*, green lines the root mean square errors *E*, and black lines the normalized standard deviation σ_f/σ_r.

dot: the more the climatological blocking pattern is similar to ERA-Interim the closer it will be to the (1,0) point. In order to provide a measure of the uncertainty of blocking frequencies in reanalysis data sets, the NCEP/NCAR Reanalysis is reported too (black triangle). It shows a standard deviation of 1.01 and a correlation of 0.99, being extremely close to the reference field.

In general, all Climate SPHINX simulations outperform the AMIP5 models. The blocking climatologies of EC-Earth have a limited spread in correlation/variance and they are locally clustered in the phase space according to resolution. However, the variability within each ensemble is nonnegligible. Indeed, T159 and T255 behave similarly so that it is hard to distinguish between these model resolutions. The first substantial improvements are seen at T511, with an increase in standard deviation and in correlation. The Pearson correlation coefficients range from 0.84 achieved by one ensemble member at T159 up to 0.95 for one T799 ensemble member.

Consistently with the blocking frequency shown in Figure 1, the T1279 simulation has a worse performance than T511 and T799. In Figure 2 it is possible to see that the distance between the T1279 simulation and any of the T511 and T799 ensemble members is larger than the distance between any pair of ensemble

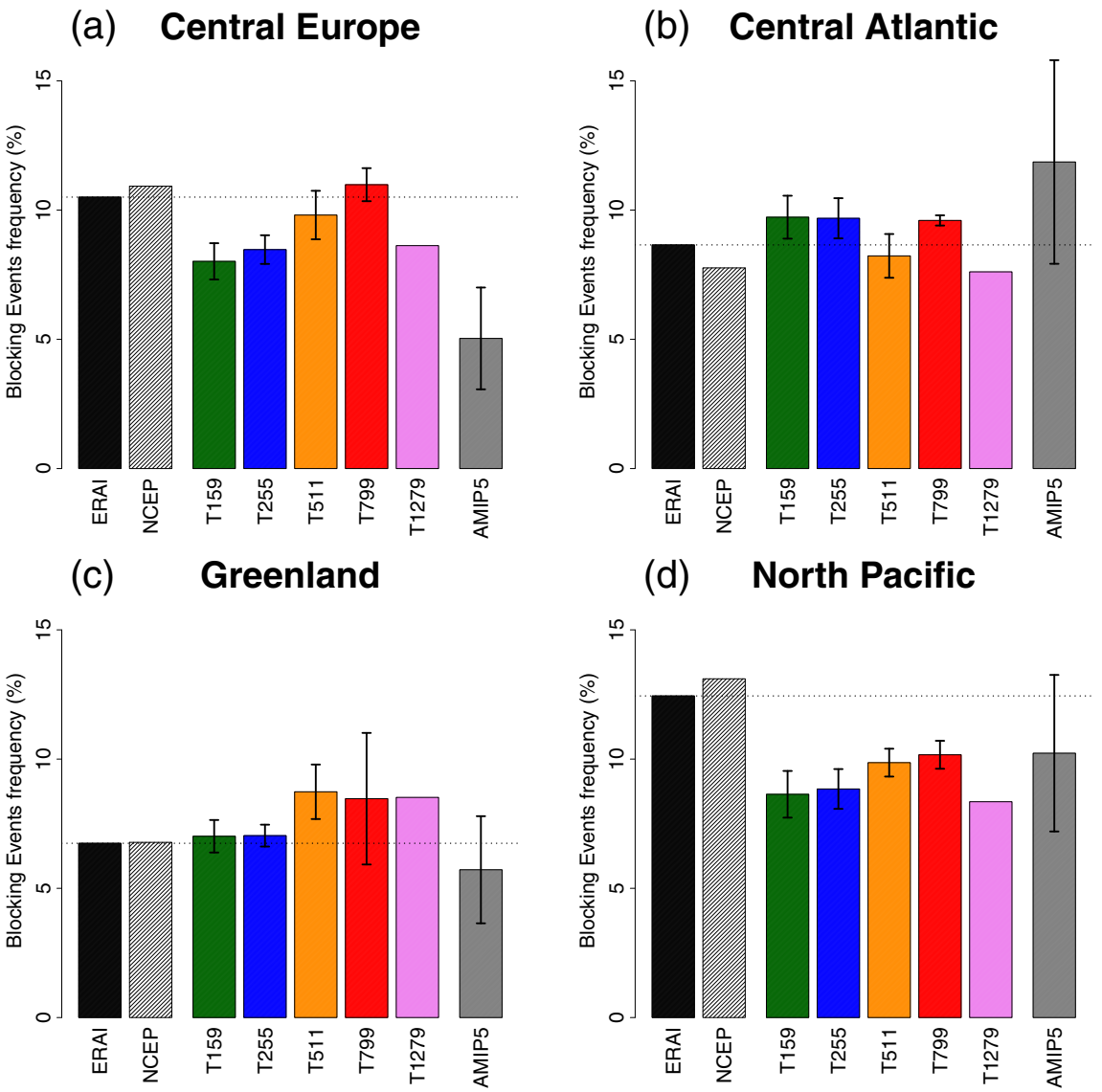

Figure 3. Blocking events frequency for ERA-Interim (black), NCEP/NCAR (dashed black) the EC-Earth ensemble mean (colors), and AMIP5 models (grey) averaged over the different regions shown Figure 1f. Error bars show the ±1 ensemble standard deviation.

members from these two latter configurations. This opens the possibility that the poor performance of the T1279 configuration may be not simply induced by the small sample examined, but that it could be linked to this specific configuration. Indeed, it should be recalled that model tuning has been carried out at T255, a resolution five times coarser than T1279.

A more detailed look at the most relevant regions of blocking occurrence is presented in Figure 3. This shows the average of the blocking frequencies over Central Europe, Greenland, Central Atlantic and North Pacific, as highlighted by the boxes in Figure 1f. The abovementioned improvement in the frequency of European blocking with resolution is apparent, occurring almost linearly up to T799. Satisfactory results with negligible bias are already obtained with the T511 version. Indeed, EC-Earth at T799 resolution is the first model to the authors' knowledge able to achieve the correct climatological blocking frequency in this region. More in general, the bias of all EC-Earth simulations is smaller than that of AMIP5.

Over the Central Atlantic (i.e., where anticyclonic low latitude wave breaking is found), EC-Earth does not show a clear dependence on resolution. Conversely, a moderate increase in blocking activity over

Greenland (i.e., where cyclonic wave breaking occurs) is observed following grid refinement. This is consistent with Figure 1, where the T511, T799 and T1279 configurations show a systematic overestimation of blocking frequency over Eastern Canada (pointing to a westward displacement of cyclonic wave breaking). However, the internal variability (especially at T799) is very large and the limited number of ensemble members might be critical to assess this quantity. Finally, Figure 3d confirms that a nonnegligible improvement is seen over the North Pacific region, where a consistent reduction of the bias is observed up to resolution T799.

3.2. Mean Model Bias

Given the important improvements observed by increasing the atmospheric horizontal resolution of EC-Earth, it is interesting to understand the mechanisms at work.

Before analyzing model changes, the biases for the "standard" T255 configuration are assessed. The mean bias of the ensemble mean of T255—compared with the reanalysis—for the Northern Hemisphere zonal mean zonal wind, temperature, and transient eddy activity is shown by colors in the upper row of Figure 4. Interestingly, EC-Earth presents a peculiar bias that could defined as a "climate-change-like" pattern. Indeed, it shows a few characteristics that are somehow shared with the predicted climate change signal. This is evident looking at the temperature bias (Figure 4b), in which the model has (a) a too weak meridional gradient of temperature at lower levels, due to an overestimation of the polar cap temperature, commonly associated with polar amplification (e.g., Cohen et al., 2014) (b) an overly strong meridional temperature gradient at upper levels associated with a too cold lower polar stratosphere and—as a consequence directly induced by thermal wind balance—a too strong and poleward displaced subtropical jet, which is usually associated with the Hadley cell response to greenhouse gases increase (e.g., Johanson & Fu, 2009).

This above described bias is more marked over the Pacific sector (not shown) and it might explain the chronic bias in the Pacific blocking frequencies seen in all configurations. Such excess of potential energy in the upper levels of the troposphere is thus likely the reason behind the observed overestimated variance of the synoptic eddies (Figure 4c). Other quantities, as the upper tropospheric eddy kinetic energy or the Eady growth rate (not shown), confirm this global overestimation of high-frequency energy, especially over the Pacific basin. On the contrary, zonal winds present smaller biases over the Atlantic ocean, with low level

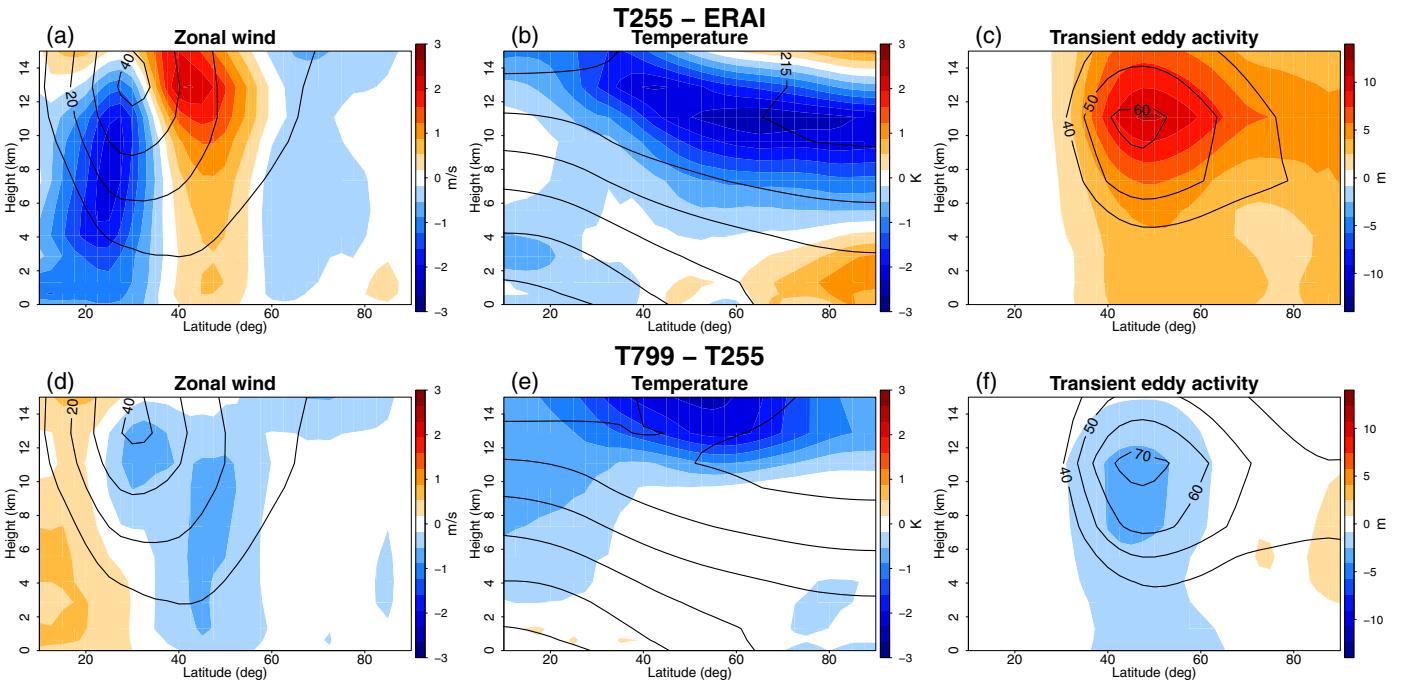

Figure 4. (a–c) Zonal mean cross sections for T255 ensemble mean bias (colors) with respect to ERA-Interim (contours) for (a) zonal wind, (b) temperature, and (c) transient eddy activity. (d–f) Same as upper row (a–c) but with T799 ensemble mean minus T255 ensemble (colors) and T255 ensemble mean (contours).

transient meridional heat fluxes which are slightly too strong over the North American East coast and too weak over the ocean (not shown).

3.3. Large-Scale Changes: An Upper Tropospheric Wave

Since an extensive comparison of the resolution-dependent changes of all EC-Earth configurations would be overly long to be included in the manuscript, the presentation is limited to the comparison of the ensemble means of the T799 and of the T255 configurations. The former would then be a reference for the "high-resolution"—since it provides three ensemble members and has the best simulated blocking frequency—while the latter is the standard "low-resolution" tuned EC-Earth version. However, it is important to stress out that our findings are similar when any permutation of a higher-resolution version (T799 and T511) versus a lower-resolution version (T255 and T159). The only exception is the T1279 simulation, that, as already stated, behaves in a peculiar way.

The same comparison performed to identify the T255 bias against reanalysis (i.e., zonal mean vertical cross-sections) is plotted in the lower row of Figure 4, showing the differences between the T799 and the T255 configurations (in colors). It is possible to see that at high resolution there is a weak but vertically extended decrease of the zonal wind (Figure 4d). Even if the zonal mean temperature is dominated by a further stratospheric cooling, the equatorial midtropospheric cooling observed in the T799 configuration has the net effect of reducing the pole-to-equator gradient. This explains why the T799 shows an upper-tropospheric reduction of the zonal wind and of the eddy transient activity (Figure 4f). Although it is not straightforward to investigate the origin of this change, this should be connected to the new radiative balance that is set in the high-resolution version. However, this decrease is barotropic throughout the column, suggesting that something is occurring also at lower levels: this change cannot simply be explained by the thermal wind balance.

A more detailed look at the changes between the T799 and the T255 can be appreciated in Figure 5, where the differences between the two model configurations for several horizontal fields are shown. The most evident element emerges when looking at the zonally asymmetric component of the upper tropospheric stream function (Figure 5a). Here a wave train propagating in the upper troposphere can be clearly spotted, showing a wave 2 pattern, characterized by a strong ridge over the Rockies and weakening downstream. This is undoubtedly the most prominent feature of the resolution increase, and it is present also in the T511 and T1279 configurations (not shown). Furthermore, the ridge over the Eastern North Atlantic suggests an increase of the amplitude of the stationary wave over Northern Europe. Indeed, this in agreement with the stronger ridges over Europe and the Rocky Mountains already shown by Davini et al. (2017) and with the increase of European blocking frequencies seen above.

The circulation anomaly associated with the abovementioned wave—stronger over North America—advects warm air poleward from lower latitudes, bringing an extensive warming (about a couple of degrees) over the western coast of North America, from California to Alaska (Figure 5b). Similarly, the stronger meridional component of wind leads to a cooling downstream over Eastern Canada. Further East, a widespread cooling is observed over Eastern Siberia.

As already highlighted by the zonal means in Figure 4, the T799 configuration has considerable weaker jet streams. This weakening is especially evident in the exit region of the Atlantic eddy-driven jet (Figure 5d) where the reduction is found also at the upper levels (Figure 5c), but a weaker jet is observed also over the Pacific basin (Figure 5c). Due to the reduced meridional temperature gradient (shown in Figure 4), transient eddies are appreciably weakened too (Figure 5f).

Finally, Figure 5e shows also that considerable changes of precipitation (on the order of several millimeter/day) are occurring in the equatorial region. This can have an important impact on the extratropical climate and it will be discussed in detail later.

3.4. North Atlantic Changes: A Weakened Storm Track

Before investigating the origin of the upper tropospheric wave seen in Figure 5a, it is interesting to analyze the dynamical connection between the stream function anomaly that peaks over the Rockies and the increased blocking frequency over Europe. This can be better appreciated looking at the cross section of zonal wind, temperature, and the Eady growth rate right upstream and downstream of the mountain range (Figure 6).

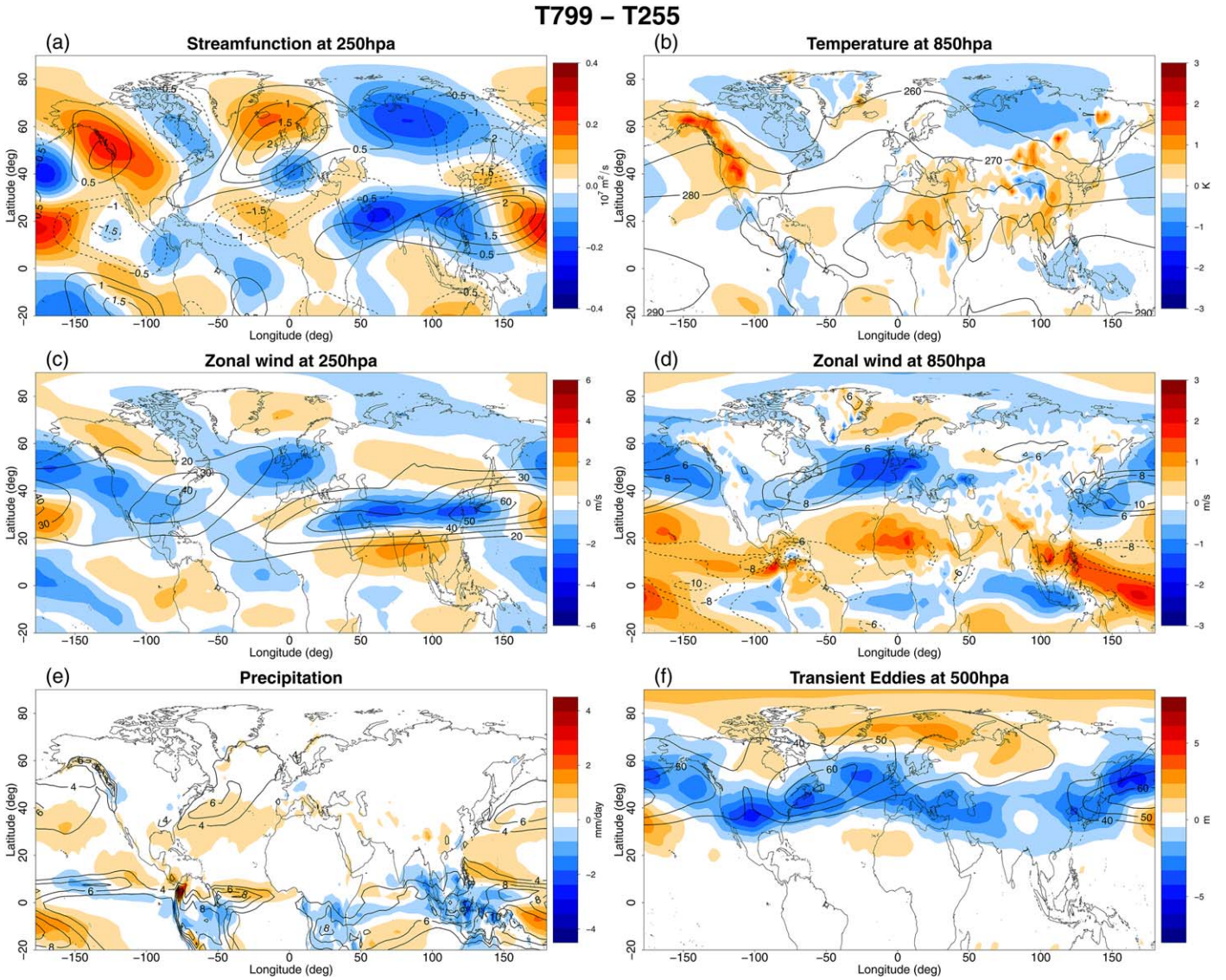

Figure 5. T799 ensemble mean minus T255 ensemble (colors) and T255 ensemble mean (contours) for (a) 250 hPa asymmetric component of stream function (b) 850 hPa temperature (c) 250 hPa zonal wind (d) 850 hPa zonal wind (e) total precipitation (f) and 500 hPa transient eddy activity.

Figure 6a shows a dipole in the zonal wind, showing that the Pacific jet is already displaced poleward between 150°W–120°W. However, such wind dipole is asymmetric, highlighting that—in addition to the poleward displacement—the jet speed is reduced too. At the first-order this weakening is due to the smaller upper tropospheric temperature gradient in the region of its largest values (Figure 6b), again reflecting the hemispheric change in the polar-to-equator gradient seen in Figure 4.

The weakened and poleward diverted jet warms Western North America advecting warmer air from lower latitudes over the Rockies (Figure 6b). The meridional temperature profile is then modified also in the lower-middle troposphere, changing the local baroclinicity, here measured by the Eady growth rate (Figure 6c). This is characterized by a decrease in the region of its maximum values and by an increase more to the north: due to the exponential character of the baroclinic growth, the decrease in the core region is more important and could explain why the kinetic energy of the transient eddies is reduced as a whole (Figure 6d).

The poleward displacement of the jet is evident also downstream of the mountain range, over the Great Plains between 100°W and 80°W (Figure 6e). Here the weaker baroclinicity is seen also in its core region at

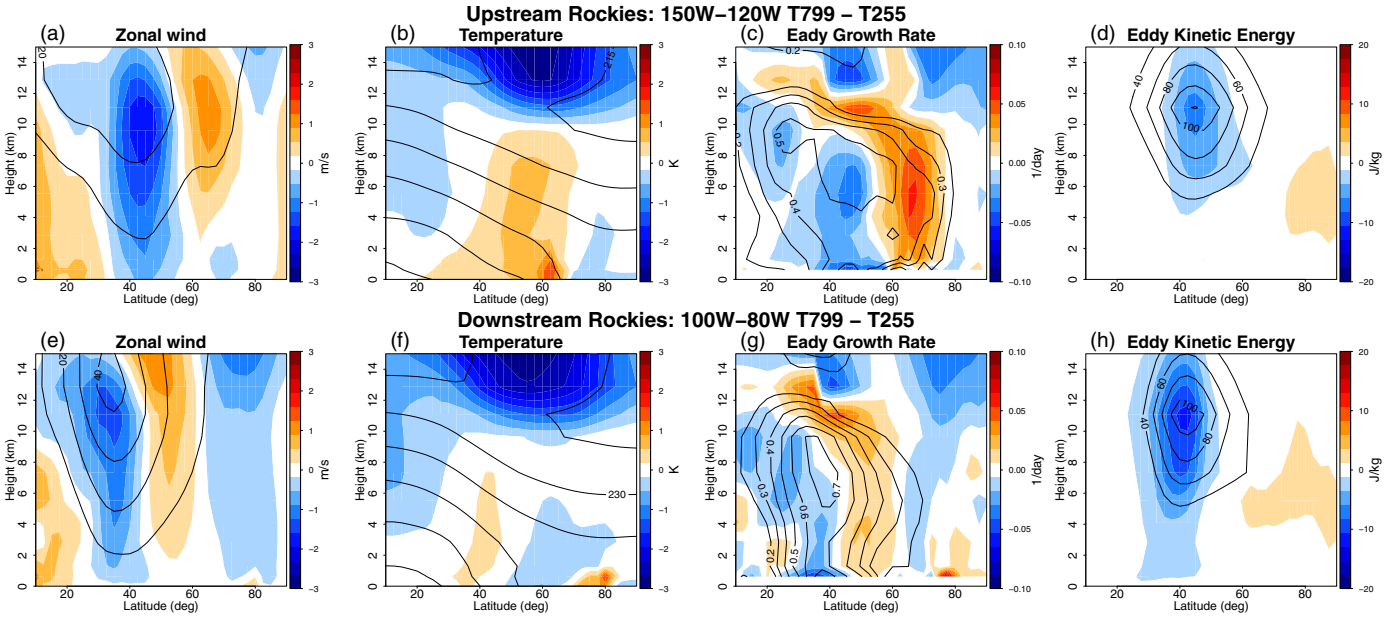

Figure 6. T799 ensemble mean minus T255 ensemble (colors) and T255 ensemble mean (contours) of zonally averaged vertical cross section for zonal wind, temperature, Eady growth rate and eddy kinetic energy (a–d) upstream of the Rocky Mountains (150°W–120°W) and (e–h) downstream of the Rocky Mountains (100°W–80°W).

lower levels (Figure 6g). As a consequence, the eddy kinetic energy is further reduced (Figure 6h), preparing the ground for the weakening of the Atlantic eddy-driven jet shown in Figure 5c.

A deeper insight is provided by Figure 7, which displays the upper and lower tropospheric changes of high-frequency eddy kinetic energy, heat fluxes, and barotropic and baroclinic conversion terms.

$\boldsymbol{E} \cdot \boldsymbol{D}$ corresponds to the barotropic energy conversion from the eddy kinetic energy to the mean flow and it reaches highest values in the upper troposphere. As mentioned above, it describes whether the jet stream is feeding the eddies (when it is positive) or the mean flow is extracting energy from the eddies (when it is negative). On climatological average (contours in Figure 7c), it is positive right after the Rockies and it is negative over the Atlantic, where the storms barotropize the flow giving rise to the eddy-driven jet stream.

On the other hand, the baroclinic conversion term F is the corresponding term for baroclinic energy. It is generally positive and describes regions where the eddies are sustained by the mean state, exploiting the meridional temperature gradient which serves as an energy source for the eddies.

As shown in Figure 6, the weaker Pacific meridional temperature gradient reduces the intensity of the storms propagating over the Eastern Pacific. As a consequence, synoptic disturbances exiting the Pacific storm track approach the North American continent with less eddy kinetic energy (Figure 7a). This clearly reduces the number of available seeds or upper-level precursors able to trigger cyclogenesis over the lee side of the Rocky Mountains.

Moreover, the $\boldsymbol{E} \cdot \boldsymbol{D}$ term (Figure 7c) shows significant smaller values downstream of the mountains (in a region of climatological positive values) suggesting that in the T799 configuration the eddies are also less effective in extracting energy from the mean flow. A deeper inspection of $\boldsymbol{E} \cdot \boldsymbol{D}$ terms (not shown) suggests that the origin of this decrease is mainly associated with a change in the longitudinal term $E_x D_x$, i.e., namely the stretching term. This means that the shape of the synoptic eddies is changed, more specifically that in the T799 configuration they are more isotropic and less meridionally stretched (eddies isotropy is related to the longitudinal component of $\boldsymbol{E}$). Less meridionally stretched eddies are less effective in mixing the meridional temperature differences, reducing the meridional heat flux $v'T'$ term as well (Figure 7b). In addition, the poleward displacement of the jet reduces the lower tropospheric temperature gradient downstream of the Rockies (Figure 5b). Consequently the baroclinic conversion of potential energy from the mean flow to the eddies—measured by F—is reduced by almost 20% (Figure 7d).

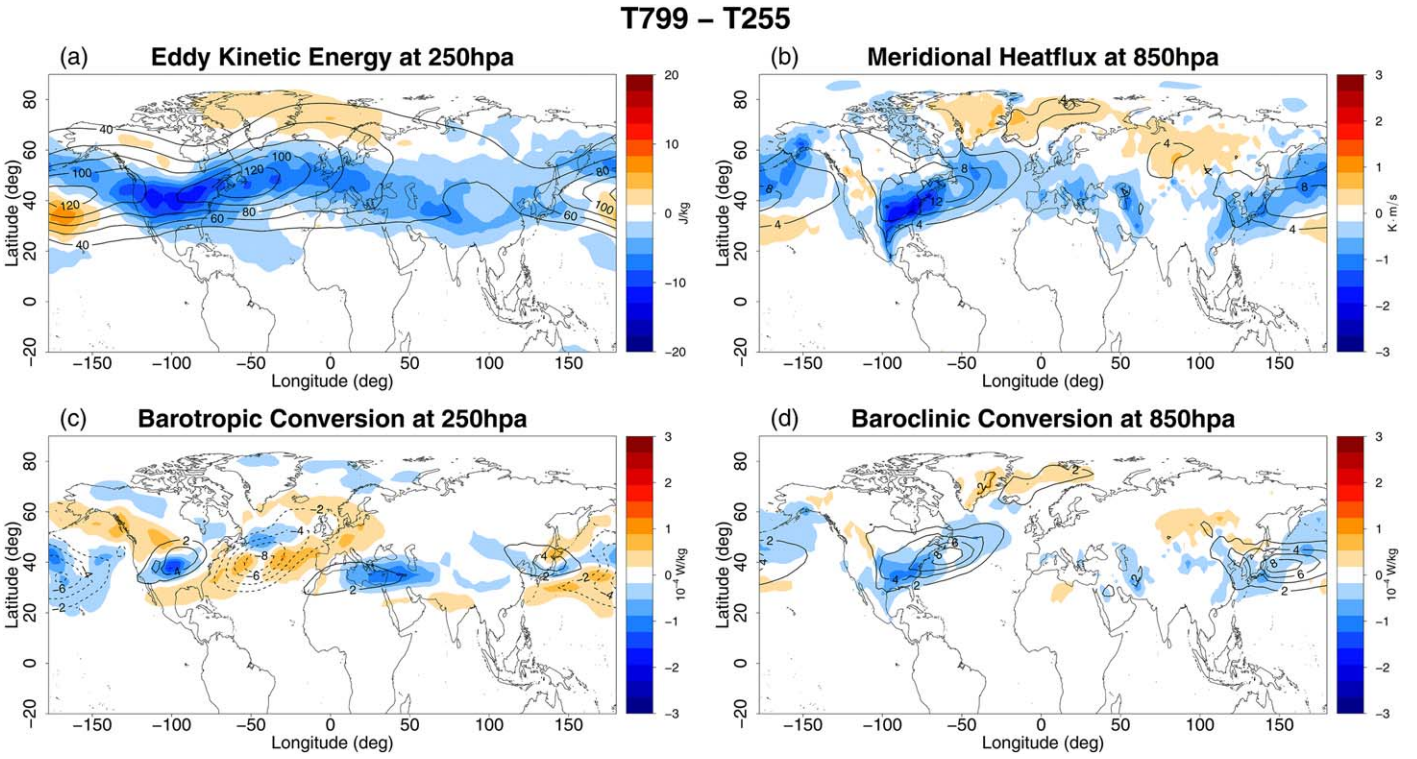

Figure 7. T799 ensemble mean minus T255 ensemble (colors) and T255 ensemble mean (contours) for (a) 250 hpa eddy kinetic energy; (b) 850 hPa transient heat flux ($v'T'$); (c) 250 hPa barotropic conversion term ($\boldsymbol{E} \cdot \boldsymbol{D}$); and (d) 850 hpa baroclinic conversion term (F).

Both the barotropic and baroclinic contribution results in less energetic eddies that are less effective in producing the eddy-driven component of the Atlantic jet. Indeed, the storm track of the T799 configuration is considerably less intense and has less energy to "barotropize" the flow (shown by positive anomalies of $\boldsymbol{E} \cdot \boldsymbol{D}$ in the central Atlantic, Figure 7c), causing slower speed and the retraction of the whole jet (Figure 5d). As a final consequence, the less effective "barotropic decay" (Chang et al., 2002) weakens the upper level jet, as shown in Figure 5c.

We therefore conclude that the weaker baroclinicity and the poleward displacement of the jet observed right upstream of the Rocky Mountains in the T799 configurations acts in (a) weakening the intensity of the upper tropospheric disturbances capable to trigger the cyclogenesis over North America and in (b) reducing the anisotropy of the synoptic eddies making baroclinic and barotropic energy conversion less effective. This leads to a considerably weaker North Atlantic storm track.

But how can a weaker Atlantic jet imply higher European blocking frequency? Several dynamical studies with simplified models have shown that in presence of a weaker jet (i.e., where the potential vorticity gradient is weaker) the frequency of Rossby wave breaking is increased (Nakamura, 1995; Peters & Waugh, 1996). Indeed Rossby wave breaking occurs preferentially in region of sustained diffluence (Tyrlis & Hoskins, 2008b), and the T799 Atlantic jet—weakened especially in its exit part—is clearly fitting with this view (Figure 5). Furthermore, the reduction of the jet speed is not caused by the increase of blocking frequency itself, because the jet speed changes are observed also when European blocking days are removed from the climatological mean (not shown).

More in general, shifting westward the zone of diffluence anticipates the region where the stretching of the eddies is occurring: this means that the synoptic waves traveling the Atlantic sector encounter larger possibility of breaking earlier (i.e., more over the ocean and less over land). This is in agreement with what seen in the blocking climatology of Figure 1. The T255 configuration shows a slight overestimation of blocking events over the Western Russia (around 30°E–60°E, 40°N–60°N): this is reduced in the higher-resolution configurations. On the contrary, blocking events over Eastern Canada and Greenland increase.

3.5. Causes of the Upper Level Wave: Mean Wind, Orography, and Precipitation

It is now crucial to investigate the origin of the increased amplitude of the planetary waves observed in the high-resolution configurations.

Already presented in section 3.3, one of the most relevant differences between the high-resolution and the low-resolution is the weaker upper level pole-to-equator temperature gradient. Figure 4 shows that the T799 is characterized by a globally weaker jet stream. This is confirmed locally by its eddy-driven and subtropical components, both weaker on the Atlantic and the Pacific basins (Figures 5c and 5d). Given the importance of such a reduced meridional gradient for the baroclinicity and the cyclogenesis—discussed in section 3.4—this might be a primary element leading to the increase of blocking frequency at T799.

However, the weaker meridional temperature gradient cannot explain the northward displacement of the Pacific jet and—more in general—the upper level wave observed in Figure 5a. As mentioned in the introduction, an improvement in blocking following resolution increase has been often associated with a more detailed (i.e., higher) mean North American orography, which leads to an increased amplitude of the planetary waves (Berckmans et al., 2013; Jung et al., 2012). Indeed, the T799 model has a resolved mean orography over the North American continent that is much more defined, as shown in Figure 8, and it is thus important to explore this possibility.

The impact of orography on the downstream flow is a broad subject widely discussed in literature (e.g., Cook & Held, 1992; Lee & Mak, 1996; Valdes & Hoskins, 1989). For instance, Held et al. (2002) showed that the impact of the Rocky Mountains is characterized by an upstream positive stream function anomaly followed by a downstream negative anomaly. A comprehensive analysis of the Rocky Mountains effect on the North Atlantic storm track has been given by Brayshaw et al. (2009) using a simplified GCM configurations with and without the North American orography. They showed how a mountain range positioned over North America creates an orographic wave characterized by an upper level positive stream function anomaly and by a local upstream warming followed by a downstream cooling (caused by the meridional displacement of the air forced by the orographic barrier). All these results are in agreement with our findings, including the positive stream function anomaly over the Rockies seen in Figure 5a as well as the temperature dipole of Figure 5b.

However, opposite to our simulations, Brayshaw et al. (2009) observed a more intense storm track and reinforced baroclinicity over the Eastern North American coast. As discussed in section 3.4, the observed weakening of the storm track in the T799 runs is strongly associated with an overall reduction of the baroclinicity. Nonetheless it should be remarked that even if a comparison between our results and those

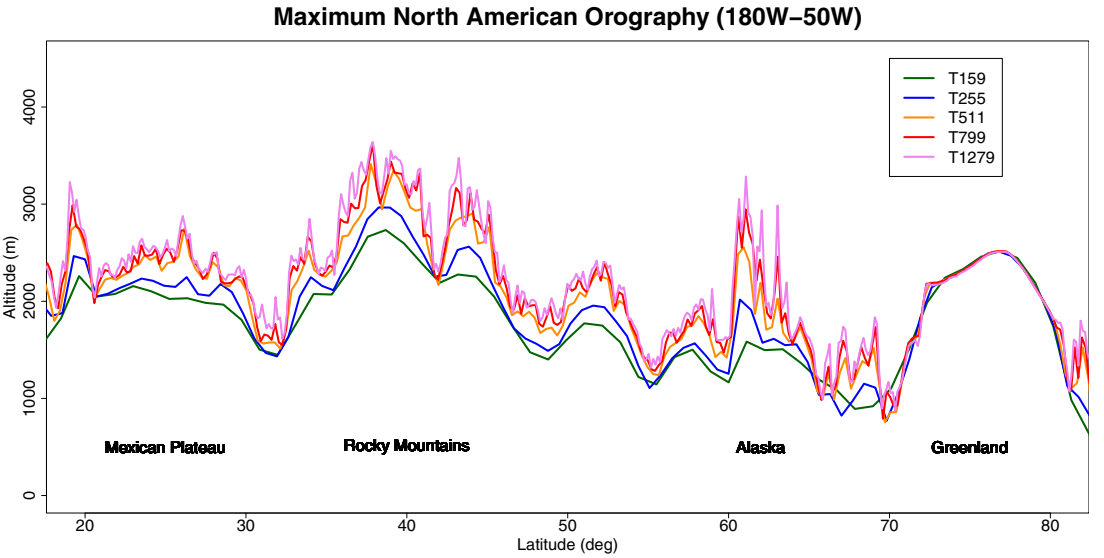

Figure 8. Meridional profile of maximum mean orography over North America (between 180°W and 50°W) at different model resolutions.

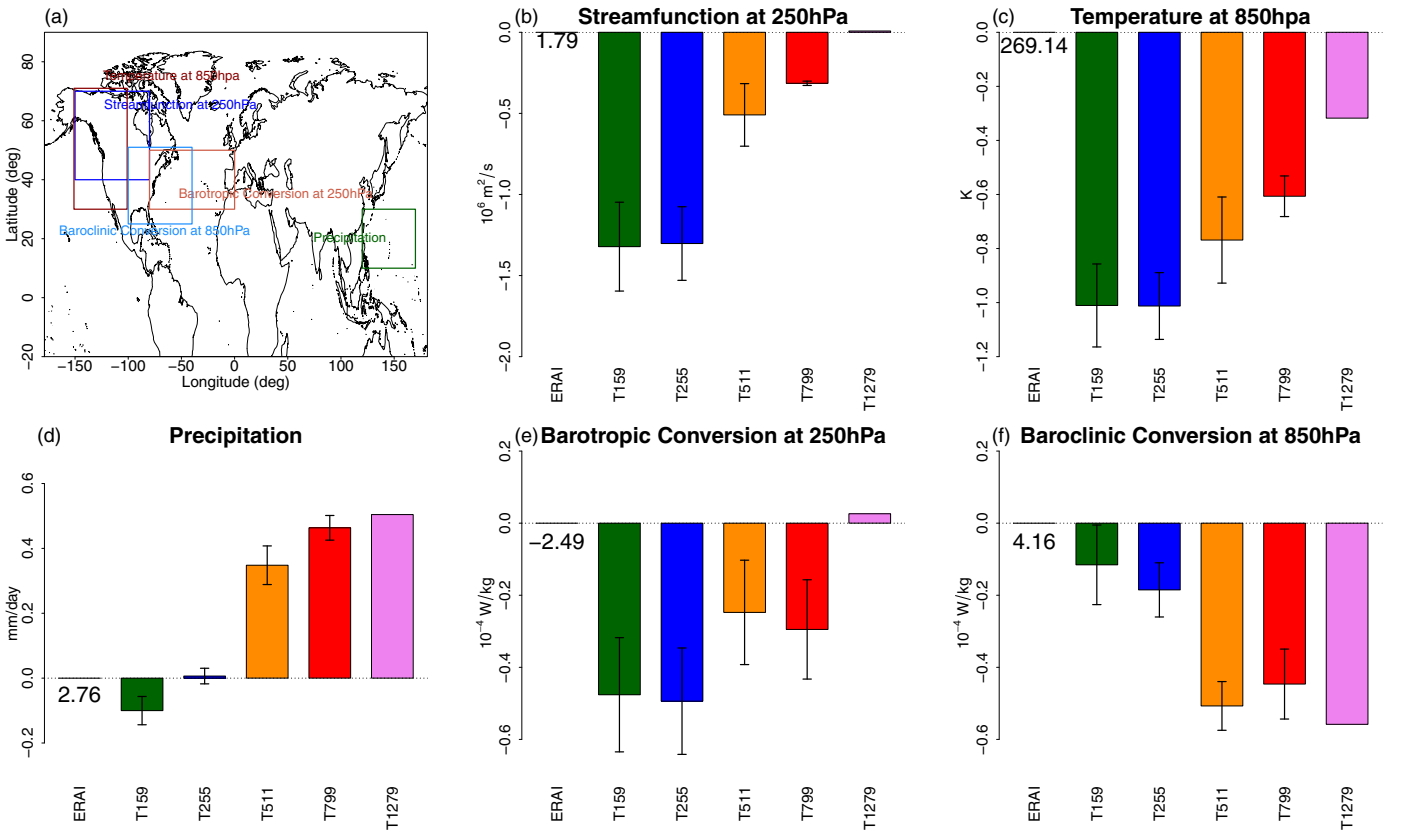

Figure 9. (a) Geographical location of the box averages used in this figure. (b–f) Box-averaged biases relative to ERA-Interim reanalysis for (b) North West American 250 hPa eddy stream function (c) North West American 850 hPa temperature (d) Philippine Sea precipitation (e) Central Atlantic 250 hPa barotropic conversion term (f) Western Atlantic 850 hPa baroclinic conversion term (f). The ERA-Interim box-averaged value is reported on the left of each plot. Error bars show the ±1 ensemble standard deviation.

previous works (e.g., Brayshaw et al., 2009; Held et al., 2002; Valdes & Hoskins, 1989) is undoubtedly fruitful, our simulations are inherently different. First, we use a full GCMs including thus a higher degree of complexity. Second, they performed sensitivity ideal experiments removing the entire Rocky Mountains, while in our case the difference (between T255 and T799) is limited to a moderate increase of the mean orography.

In order to get more insight on this aspect, Figure 9 shows the comparison of some specific variables averaged over their relevant regions (shown in Figure 9a) for all the resolutions used in SPHINX. Figure 9b shows the dependence on resolution of the anomalies of the 250 hPa stream function over Western North America. At lower resolution, the model shows a negative bias against ERA-Interim, that is gradually reduced increasing the resolution, with a significant improvement passing from T255 up to T511. This is the resolution change for which the blocking bias is most strongly reduced (Figure 3) and for which the definition of the orography is most notably improved (Figure 8). In a similar way, the negative bias in the lower tropospheric temperature, which is tightly associated with the poleward advection of warm air over the upstream side of the Rockies and thus with the orographic effect, decreases increasing the resolution (Figure 9c). This linear dependence between orography, stream function, and temperature puts extra evidence on the relationship between the observed poleward displacement of the jet and the resolution of the orography.

A further support to the hypothesis of the dominant role of orography comes from Jung et al. (2012) and Berckmans et al. (2013). They both assessed the role of the resolution of orography on atmospheric blocking by comparing the same GCM in three different configurations: high-resolution, low-resolution, and one where the high-resolution GCM is run with a low-resolution orography. Both studies showed that the improvements in blocking frequencies achieved by the high-resolution configuration vanished when the low-resolution orography was used. The work of Jung et al. (2012) (see their Figure 8c) is especially relevant

for the present study because they used an older version the ECMWF model, that shares large portions of the code with the EC-Earth version used for Climate SPHINX.

Tropical diabatic heating deserves a final comment: an intense change in precipitation, as the one observed between the T799 and T255 configurations in the Western Pacific (Figure 5e), is known for being able to trigger Rossby wave trains that propagate poleward up to the extratropics (Hoskins & Karoly, 1981). This has proven to be able to influence European climate and potentially blocking frequencies (Cassou, 2008; Henderson et al., 2016). As shown by Figure 9d, also the increase of precipitation over tropical Western Pacific is proportional to resolution.

Nonetheless there are a couple of reasons why this should be considered as unlikely: even if wave trains generated by change in deep convection depends strongly on the mean flow (a) these waves do not usually have the capacity to circumnavigate the whole globe (Jin & Hoskins, 1995) (b) they have usually a higher wavenumber, on the order of k = 5–6 versus k = 2 in EC-Earth simulations (Ambrizzi & Hoskins, 1997; Hoskins & Ambrizzi, 1993).

However, considering the fact that the ECMWF model is known to have a pronounced sensitivity to tropical forcing (e.g., Jung et al., 2010b) precipitation might represent an additional mechanism that—interacting non-linearly with the increase of mean orography—may be able to weaken and shift poleward the Pacific jet generating thus the observed upper level stream function anomaly.

3.6. Correct Blocking Frequencies for the Wrong Reasons

Looking back at Figure 4b, it is possible to see that from an energetic point of view EC-Earth is characterized by an overestimation of the potential energy available in the upper tropospheric levels—due to the overly strong meridional temperature gradient. This is in turn followed by too strong upper level transient eddies (Figure 4c). Even if this potential energy available is reduced at T799, there is still an evident overestimation of both variables (Figures 4e and 4f).

Conversely, the lower level baroclinicity is reasonably well represented at T255 and it becomes too weak at T511, T799, and T1279. This can be appreciated looking at the baroclinic conversion term over Western North Atlantic (i.e., where baroclinicity is stronger) in Figure 9f, that is showing a decrease of 10–15% in the higher-resolution configurations. The contribution from the barotropic term over Central North Atlantic, shown in Figure 9e, is also less important, with its magnitude reduced by more than 25%, suggesting that eddies are no longer able to sustain the Atlantic jet stream. It is important to point out that even if the bias of the barotropic conversion term against ERA-Interim reanalysis is now smaller, the high-resolution configurations show an overall reduction in the amplitude of both baroclinic and barotropic energy conversion. At high resolution, the Atlantic eddies are thus weaker than at low resolution, and consequently the Atlantic jet stream, that shows a small bias at T255, is characterized by a larger negative bias at higher resolution (T511, T799, and T1279).

Therefore, even though the T511 and T799 configurations show a representation of blocking events frequencies over Europe with negligible biases, they present a too weak Atlantic storm track and eddy-driven jet. This is somewhat counterintuitive: in general one may think that a higher-resolution simulation should be characterized by stronger and/or more frequent transient eddies (e.g., Guemas & Codron, 2011). The lack of such findings forces us to conclude that the correct blocking frequency simulated by the T799 configuration is due to wrong reasons, likely following bias compensation.

Figure 10 shows that the T511 and T799 resolution configurations (characterized by a correct blocking frequency) underestimate the blocking duration in favor of an overestimation of the number of blocking events. Indeed, even the best simulation run at T799 (red dots) is unable to level out the blocking duration observed in ERA-Interim Reanalysis (black dot) or in NCEP/NCAR Reanalysis (black triangle). Conversely there are four simulations that clearly overestimate the number of blocking events. This peculiar EC-Earth bias is well represented by the linear regression between the ensemble mean duration and the ensemble mean number of events, showed by the dotted line in Figure 10.

The onset of a blocking event is usually associated with Rossby wave breaking: this occurs more easily in zone of diffluence, i.e., where the jet is weaker (Peters & Waugh, 1996). Conversely, blocking maintenance mechanisms are likely associated with the presence of transient eddies (e.g., Shutts, 1983). The results from Figure 10 fit well with this interpretation. Over the North Atlantic, the T799 underestimates the magnitude

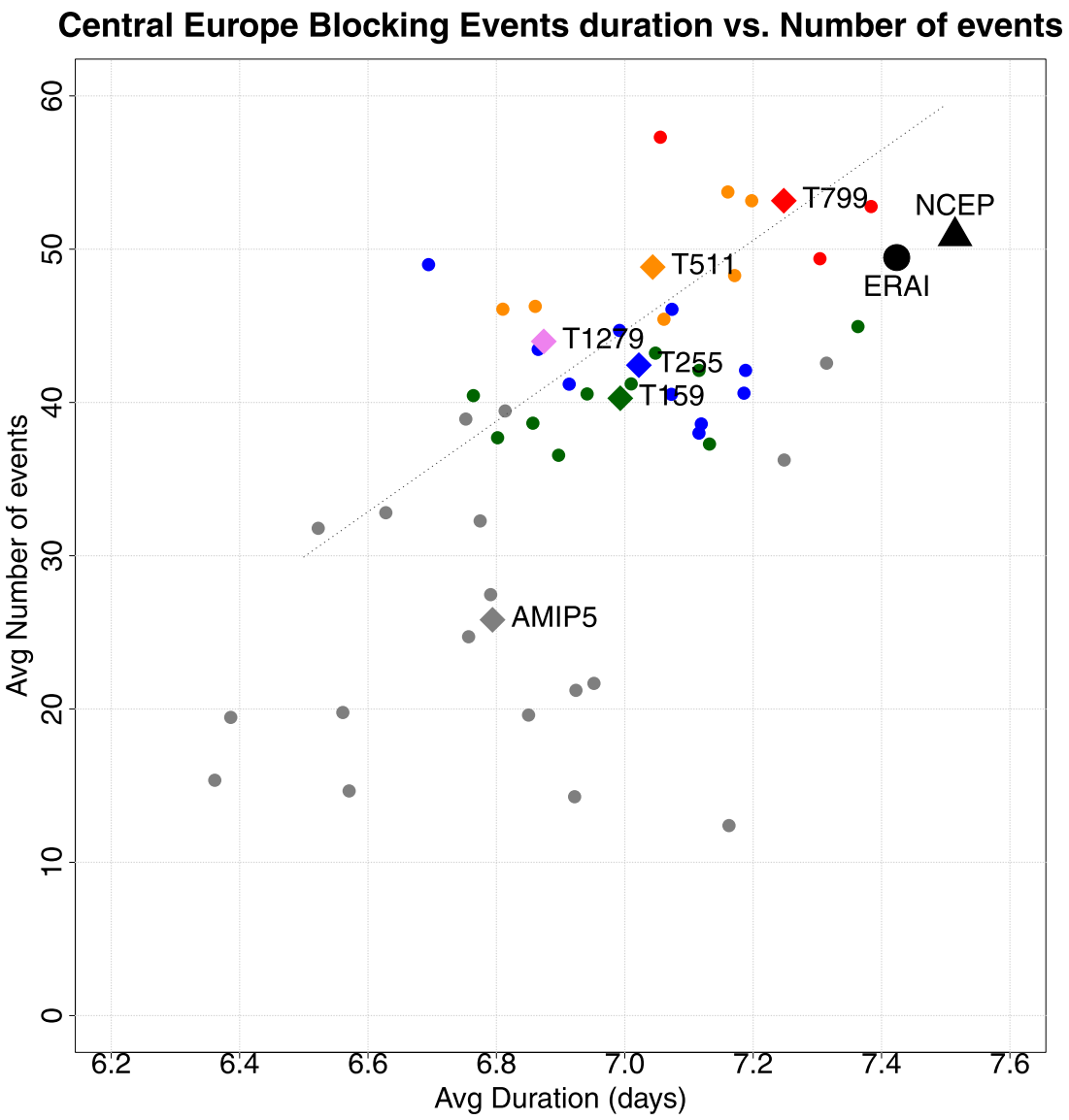

Figure 10. Blocking events duration versus number of blocking events averaged over the European sector as shown by Figure 1f. Each dot is an ensemble member, diamonds are the ensemble mean. The black dot is ERA-Interim, black triangle is NCEP/NCAR. The linear regression of the EC-Earth ensemble means is shown by the dashed line.

of the transient eddies (which could reduce the duration of blocking events) and of the mean jet speed (which could favor an overestimation of Rossby wave breaking events, i.e., increasing the number of European blocking onset).

Finally, this "correct blocking for wrong reasons" example may help us to interpret the unexpected behavior of the T1279. At T255 EC-Earth is characterized by a too weak meridional temperature gradient at lower levels and by a too strong one at upper levels (Figure 4b). The more the EC-Earth resolution is increased, the more the model experiences an almost vertically uniform decrease in transient eddy energy. However, it still maintains this incorrect distribution between upper and lower levels. Less energy available leads to a slower Atlantic jet stream, which favors the correct European blocking frequencies at T511 and at T799. However, at T1279 the resolution-induced effects have become too prominent: the baroclinic transient eddies are overly reduced (see Figures 9e and 9f) and this affects the average position of the jet, possibly leading to the observed underestimation of European blocking frequency.

4. Discussions and Conclusions

A large set of atmospheric-only climate simulations at five different horizontal resolutions with the EC-Earth Earth System Model has been analyzed to evaluate the impact of increased resolution in simulating the atmospheric blocking. Results show that at lower resolutions (T159–T255, i.e., 125–80 km) EC-Earth underestimates blocking frequencies over both Europe and North Pacific (Figures 1f and 1g). The negative bias over Europe is however less pronounced than in the majority of AMIP5 models (Figure 3a).

When the EC-Earth horizontal resolution is increased to 40 km (T511) and 25 km (T799), the Pacific bias is almost halved (if compared to T159 and T255). Most importantly, the European blocking frequency bias is reduced to the point that it can be confidently considered as negligible—especially at T799.

Such a dramatic improvement in the frequencies of blocking events seems to be mainly caused by two concurring factors. (a) Following the grid refinement, a different radiative balance is set causing a reduction of the upper tropospheric pole-to-equator gradient, more prominent over the Pacific and the Atlantic sector. This leads to a reduction of the upper level baroclinicity, which weakens the jet streams and reduces the eddy kinetic energy. (b) The higher resolution implies a more refined—and thus higher—mean orography which (possibly in association with a change in tropical precipitation), forces a stationary planetary wave, which deflects northward the jet stream over the Rocky Mountains. This in turn changes the meridional temperature gradient over North America, further affecting the position and the speed of the Atlantic jet stream.

These two factors lead to a decrease of both barotropic and baroclinic energy conversion and to a reduction of the eddy efficiency in extracting energy (due to the less meridionally stretched eddies in the high-resolution configurations). The Atlantic storm track and the Atlantic jet stream are consequently weakened, especially in their exit region. This results in a less sharp potential vorticity gradient over North Atlantic which favors the occurrence of Rossby wave breaking in the diffluence region of the jet—which is now displaced westward—increasing the number of onsets of blocking there. Indeed, EC-Earth high-resolution configurations show not only an increase in European blocking frequencies but also a slight overestimation of blocking events over Western Greenland and Eastern Canada, pointing to a basin-wide westward displacement of wave breaking activity.

However, this is only one side of the coin: if compared to reanalyses, the T511 and T799 resolution configurations show that correct blocking frequencies are achieved with an overestimation of blocking onsets that compensates an underestimation of the blocking duration. This behavior can be explained looking at the T511 and T799 biases over the North Atlantic: they are both characterized by a jet stream that is too weak (which, reducing the potential vorticity gradient, should favor an overestimation of the number of blocking onsets) and by too weak transient eddies (which should favor the underestimation of the blocking duration).

Ultimately, it appears clear that correct blocking frequencies are achieved through bias compensation between the eddies found at upper levels (too strong) and at lower levels (too weak). This interpretation may provide an explanation of why the highest resolution (T1279) shows worse results than T799 and T511. The overly strong upper level eddy activity (seen in all the EC-Earth configurations) may be compensated, up to a certain amount (i.e., in the T511 and T799), by a weak low level baroclinicity, decreasing the Atlantic jet speed and increasing the blocking frequencies. However, if the eddies are too weak (as in the T1279) blocking is no longer sustained. This can be thought as an analogy to what occurs in summer, where the jet stream is weaker (and displaced poleward) and blocking frequencies are considerably lower.

The observed winter blocking frequencies appears to be a specific solution of the "climate model phase-space": on the one side, when the Atlantic jet is too strong, no wave breaking occurs as in many CMIP5 models (Anstey et al., 2013). On the other side, if the jet is too weak then wave breaking is misplaced in the Euro Atlantic basin, leading to a strong bias in blocking events frequencies (see MIROC5 GCM in Anstey et al., 2013). More in general, these findings suggest three main considerations:

1. The "correct blocking frequency" is not necessarily the result of a more realistic simulation of the atmospheric dynamics: a numerical model can achieve several error compensations in its internal dynamics of the jet stream, which may lead to a perfect blocking frequency even if other elements of the large-scale dynamics present substantial biases.

2. Horizontal resolution may not be the unique remedy to obtain an unbiased blocking frequency. Even if the better representation of orography associated with the increase in resolution represents of course a crucial component, the good results of the EC-Earth T799 configuration are to a large extent associated with the weakening of the Atlantic storm track. This is clearly not due to some specific feature of high horizontal resolution. Indeed, this weakening could be potentially simulated with improved subgrid orography-related parameterizations (Pithan et al., 2016; Sandu et al., 2016), or perhaps with a more precise simulation of the meridional temperature gradient.
3. It has been long claimed that transient eddies can be obtained only with high resolution and that they are fundamental for blocking simulations (e.g., Berckmans et al., 2013; Shutts, 1983). In the EC-Earth simulations transient eddies are still underestimated even at 16 km resolution, suggesting that they are not necessarily better represented at higher resolution. However, the observed underestimation of duration puts a further element in favor of the relevance of transient eddies in the blocking maintenance mechanisms.

To conclude, this analysis shows that huge improvements can be achieved in simulating atmospheric blocking with the help of high resolution, but many further issues should be addressed in order to disentangle the different mechanisms and unveil the driving dynamics of blocking onset/maintenance.

To this end, more targeted sensitivity experiments should be carried out to estimate the respective role of orography, subgrid-scale parameterization and climate model tuning in order to highlight what are the key physical processes whose correct simulation is relevant (if not essential) for a correct (i.e., physically sound) simulation of atmospheric blocking. More in general, this analysis suggests that there is still the need to design and setup idealized experiments, possibly with simplified GCMs, to test the blocking sensitivity to certain parameters (such as orography, SST front strength, lower and upper meridional temperature gradients, precipitation changes in specific regions).

Acknowledgments
Free data accessibility to the climate user community is granted through a dedicated THREDDS Web Server hosted by CINECA (https://sphinx.hpc.cineca.it/thredds/sphinx.html), where it is possible to browse and directly download any of the Climate SPHINX data used in the present work. Further details on the data accessibility and on the Climate SPHINX project itself are available on the official website of the project (http://www.to.isac.cnr.it/sphinx/). The authors acknowledge computing resources provided by CINECA and LRZ in the framework of Climate SPHINX PRACE project. Paolo Davini and Fabio D'Andrea gratefully acknowledge the funding from the European Union's Horizon 2020 research and innovation program COGNAC under the European Union Marie Skłodowska-Curie grant agreement 654942. Jost von Hardenberg acknowledges support from the European Union's Horizon 2020 research and innovation programme under grant agreement 641816 (CRESCENDO). Susanna Corti acknowledges support by the PRIMAVERA project, funded by the European Commission under grant agreement 641727 of the Horizon 2020 research programme. We acknowledge the contribution of the C3S 34a Lot 2 Copernicus Climate Change Service project, funded by the European Union, to the development of software tools used in this work.

References

Ambrizzi, T., & Hoskins, B. J. (1997). Stationary Rossby-wave propagation in a baroclinic atmosphere. *Quarterly Journal of the Royal Meteorological Society*, *123*(540), 919–928.

Anstey, J. A., Davini, P., Gray, L. J., Woollings, T. J., Butchart, N., Cagnazzo, C., . . . Yang, S. (2013). Multi-model analysis of northern hemisphere winter blocking: Model biases and the role of resolution. *Journal of Geophysical Research: Atmospheres*, *118*, 3956–3971. https://doi.org/10.1002/jgrd.50231

Austin, J. (1980). The blocking of middle latitude westerly winds by planetary waves. *Quarterly Journal of the Royal Meteorological Society*, *106*(448), 327–350.

Balsamo, G., Viterbo, P., Beljaars, A., van den Hurk, B., Hirschi, M., Betts, A. K., & Scipal, K. (2009). A revised hydrology for the ECMWF model: Verification from field site to terrestrial water storage and impact in the Integrated Forecast System. *Journal of Hydrometeorology*, *10*(3), 623–643.

Barnes, E. A., Dunn-Sigouin, E., Masato, G., & Woollings, T. (2014). Exploring recent trends in northern hemisphere blocking. *Geophysical Research Letters*, *41*, 638–644. https://doi.org/10.1002/2013GL058745

Barriopedro, D., Garcia-Herrera, R., Lupo, A., & Hernandez, E. (2006). A climatology of Northern hemisphere blocking. *Journal of Climate*, *19*, 1042–1063.

Barriopedro, D., Garcia-Herrera, R., & Trigo, R. (2010). Application of blocking diagnosis methods to General Circulation Models. Part I: A novel detection scheme. *Climate Dynamics*, *35*(7–8), 1373–1391.

Berckmans, J., Woollings, T., Demory, M.-E., Vidale, P.-L., & Roberts, M. (2013). Atmospheric blocking in a high resolution climate model: Influences of mean state, orography and eddy forcing. *Atmospheric Science Letters*, *14*(1), 34–40.

Berggren, R., Bolin, B., & Rossby, C. (1949). An aerological study of zonal motion, its perturbations and break-down. *Tellus*, *1*(2), 14–37.

Black, R. X., & Dole, R. M. (2000). Storm tracks and barotropic deformation in climate models. *Journal of Climate*, *13*(15), 2712–2728.

Brayshaw, D., Hoskins, B., & Blackburn, M. (2009). The basic ingredients of the North Atlantic storm track. Part I: Land-sea contrast and orography. *Journal of the Atmospheric Science*, *66*, 2539–2558.

Cai, M., & Mak, M. (1990). Symbiotic relation between planetary and synoptic-scale waves. *Journal of the Atmospheric Sciences*, *47*(24), 2953–2968.

Cassou, C. (2008). Intraseasonal interaction between the Madden–Julian oscillation and the north Atlantic oscillation. *Nature*, *455*(7212), 523–527.

Chang, E. K., Lee, S., & Swanson, K. L. (2002). Storm track dynamics. *Journal of Climate*, *15*(16), 2163–2183.

Charney, J., & DeVore, J. (1979). Multiple flow equilibria in the atmosphere and blocking. *Journal of the Atmospheric Sciences*, *36*(7), 1205–1216.

Cohen, J., J. A., Screen, J. C., Furtado, M., Barlow, D., Whittleston, D., Coumou, J., . . . Jones, J. (2014). Recent Arctic amplification and extreme mid-latitude weather. *Nature Geoscience*, *7*(9), 627–637.

Cook, K. H., & Held, I. M. (1992). The stationary response to large-scale orography in a general circulation model and a linear model. *Journal of the Atmospheric Sciences*, *49*(6), 525–539.

Davini, P., Cagnazzo, C., Gualdi, S., & Navarra, A. (2012). Bidimensional diagnostics, variability and trends of Northern hemisphere blocking. *Journal of Climate*, *25*(19), 6996–6509.

Davini, P., & D'andrea, F. (2016). Northern hemisphere atmospheric blocking representation in global climate models: Twenty years of improvements? *Journal of Climate*, *29*(24), 8823–8840.

Davini, P., Hardenberg, J. V., Corti, S., Christensen, H. M., Juricke, S., Subramanian, A., . . . Palmer, T. N. (2017). Climate SPHINX: Evaluating the impact of resolution and stochastic physics parameterisations in the EC-Earth Global Climate Model. *Geoscientific Model Development*, *10*(3), 1383–1402.

Dee, D., S., Uppala, A., Simmons, P., Berrisford, P., Poli, S., Kobayashi, U., . . .Vitart, F. (2011). The ERA-Interim reanalysis: Configuration and performance of the data assimilation system. *Quarterly Journal of the Royal Meteorological Society*, *137*(656), 553–597.

Dunn-Sigouin, E., & Son, S.-W. (2013). Northern Hemisphere blocking frequency and duration in the CMIP5 models. *Journal of Geophysical Research: Atmospheres*, *118*, 1179–1188. https://doi.org/10.1002/jgrd.50143

ECWMF (2010). *IFS cycle36r1* (technical report). Shinfield Park, Reading, UK: European Center for Medium Range Forecast. Retrieved from https://www.ecmwf.int/sites/default/files/elibrary/2010/9233-part-iv-physical-processes.pdf

Green, J. (1977). The weather during July 1976: Some dynamical considerations of the drought. *Weather*, *32*(4), 120–126.

Guemas, V., & Codron, F. (2011). Differing impacts of resolution changes in latitude and longitude on the midlatitudes in the LMDZ atmospheric GCM. *Journal of Climate*, *24*(22), 5831–5849.

Hazeleger, W., C., Severijns, T., Semmler, S., Ştefănescu, S., Yang, X., Wang, K., . . . Willén, U. (2010). Ec-earth: A seamless earth-system prediction approach in action. *Bulletin of the American Meteorological Society*, *91*(10), 1357–1363.

Hazeleger, W., X., Wang, C., Severijns, S., Ştefănescu, R., Bintanja, A., Sterl, K., . . . van der Wiel, K. *et al*. (2012). EC-Earth V2.2: Description and validation of a new seamless Earth system prediction model. *Climate Dynamics*, *39*(11), 2611–2629.

Held, I. M., Ting, M., & Wang, H. (2002). Northern winter stationary waves: Theory and modeling. *Journal of Climate*, *15*(16), 2125–2144.

Henderson, S. A., Maloney, E. D., & Barnes, E. A. (2016). The influence of the Madden–Julian oscillation on Northern Hemisphere winter blocking. *Journal of Climate*, *29*(12), 4597–4616.

Hoskins, B. J., & Ambrizzi, T. (1993). Rossby wave propagation on a realistic longitudinally varying flow. *Journal of the Atmospheric Sciences*, *50*(12), 1661–1671.

Hoskins, B. J., James, I. N., & White, G. H. (1983). The shape, propagation and mean-flow interaction of large-scale weather systems. *Journal of the Atmospheric Sciences*, *40*(7), 1595–1612.

Hoskins, B. J., & Karoly, D. J. (1981). The steady linear response of a spherical atmosphere to thermal and orographic forcing. *Journal of the Atmospheric Sciences*, *38*(6), 1179–1196.

Jin, F., & Hoskins, B. J. (1995). The direct response to tropical heating in a baroclinic atmosphere. *Journal of the Atmospheric Sciences*, *52*(3), 307–319.

Johanson, C. M., & Fu, Q. (2009). Hadley cell widening: Model simulations versus observations. *Journal of Climate*, *22*(10), 2713–2725.

Jung, T., Balsamo, G., Bechtold, P., Beljaars, A., Köhler, M., Miller, M., . . . Tompkins, A. (2010a). The ECMWF model climate: Recent progress through improved physical parametrizations. *Quarterly Journal of the Royal Meteorological Society*, *136*(650), 1145–1160.

Jung, T., Miller, M. J., & Palmer, T. N. (2010b). Diagnosing the origin of extended-range forecast errors. *Monthly Weather Review*, *138*(6), 2434–2446. http://doi.org/10.1175/2010MWR3255.1

Jung, T., Miller, T., Palmer, P., Towers, N., Wedi, D., Achuthavarier, J., . . . Hodges, K. I. (2012). High-resolution global climate simulations with the ECMWF model in project Athena: Experimental design, model climate, and seasonal forecast skill. *Journal of Climate*, *25*(9), 3155–3172.

Kalnay, E., Kanamitsu, M., Kistler, R., Collins, W., Deaven, D., Gandin, L., . . . Joseph, D. (1996). The NCEP/NCAR 40-year reanalysis project. *Bulletin of the American Meteorological Society*, *77*, 437–471.

Lee, S. (2000). Barotropic effects on atmospheric storm tracks. *Journal of the Atmospheric Sciences*, *57*(9), 1420–1435.

Lee, W.-J., & Mak, M. (1996). The role of orography in the dynamics of storm tracks. *Journal of the Atmospheric Sciences*, *53*(12), 1737–1750.

Malguzzi, P., & Malanotte-Rizzoli, P. (1984). Nonlinear stationary Rossby waves on nonuniform zonal winds and atmospheric blocking. Part I: The analytical theory. *Journal of Atmospheric Sciences*, *41*, 2620–2628.

Masato, G., Hoskins, B., & Woollings, T. (2011). Wave-breaking characteristics of Mid-latitude Blocking, *Quarterly Journal of Royal Meteorological Society*, *138*, 1285–1296.

Masato, G., Hoskins, B. J., & Woollings, T. (2013). Winter and Summer Northern Hemisphere blocking in CMIP5 models. *Journal of Climate*, *26*, 7044–7059.

Matsueda, M. (2011). Predictability of Euro-Russian blocking in summer of 2010. *Geophysical Research Letters*, *38*, L06801. https://doi.org/10.1029/2010GL046557

Matsueda, M., Mizuta, R., & Kusunoki, S. (2009). Future change in wintertime atmospheric blocking simulated using a 20-km-mesh atmospheric global circulation model. *Journal of Geophysical Research*, *114*, D12114. https://doi.org/10.1029/2009JD011919

McWilliams, J. C. (1980). An application of equivalent modons to atmospheric blocking. *Dynamics of Atmospheres and Oceans*, *5*, 43–66.

Moss, R. H., Edmonds, J. A., Hibbard, K. A., Manning, M. R., Rose, S. K., van Vuuren, D. P., . . . Wilbanks, T. J. (2010). The next generation of scenarios for climate change research and assessment. *Nature*, *463*(7282), 747–756.

Nakamura, H., Nakamura, M., & Anderson, J. (1997). The role of high- and low-frequency dynamics in blocking formation. *Monthly Weather Review*, *125*(9), 2074–2093.

Nakamura, M. (1995). *Characteristics of potential vorticity mixing by breaking Rossby waves in the vicinity of a jet* (PhD thesis, 253 pp.). Cambridge, MA: Department of Earth, Atmospheric and Planetary Sciences, Massachusetts Institute of Technology.

O'Reilly, C. H., Minobe, S., & Kuwano-Yoshida, A. (2016). The influence of the Gulf Stream on wintertime European blocking. *Climate Dynamics*, *47*(5–6), 1545–1567.

Pelly, J., & Hoskins, B. (2003). A new perspective on blocking. *Journal of the Atmospheric Science*, *60*, 743–755.

Peters, D., & Waugh, D. (1996). Influence of barotropic shear on the poleward advection of upper-tropospheric air. *Journal of Atmospheric Science*, *53*, 3013–3031.

Pfahl, S., Schwierz, C., Croci-Maspoli, M., Grams, C. M., & Wernli, H. (2015). Importance of latent heat release in ascending air streams for atmospheric blocking. *Nature Geoscience*, *8*(8), 610–614.

Pithan, F., Shepherd, T. G., Zappa, G., & Sandu, I. (2016). Climate model biases in jet streams, blocking and storm tracks resulting from missing orographic drag. *Geophysical Research Letters*, *43*, 7231–7240. https://doi.org/10.1002/2016GL069551

Rex, D. (1950). Blocking action in the middle troposphere and its effect upon regional climate: I. An aerological study of blocking action. *Tellus*, *2*, 196–211.

Riviere, G., & Joly, A. (2006). Role of the low-frequency deformation field on the explosive growth of extratropical cyclones at the jet exit. Part II: Baroclinic critical region. *Journal of the Atmospheric Sciences*, *63*(8), 1982–1995.

Sandu, I., Bechtold, P., Beljaars, A., Bozzo, A., Pithan, F., Shepherd, T. G., & Zadra, A. (2016). Impacts of parameterized orographic drag on the northern hemisphere winter circulation. *Journal of Advances in Modeling Earth Systems*, *8*, 196–211. https://doi.org/10.1002/2015MS000564

Scaife, A., Copsey, D., Gordon, C., Harris, C., Hinton, T., Keeley, S., . . . Williams, K. (2011). Improved Atlantic winter blocking in a climate model. *Geophysical Research Letters*, *38*, L23703. https://doi.org/10.1029/2011GL049573

Scaife, A., Woollings, T., Knight, J., Martin, G., & Hinton, T. (2010). Atmospheric blocking and mean biases in climate models. *Journal of Climate*, *23*, 6143–6152.

Scherrer, S., Croci-Maspoli, M., Schwierz, C., & Appenzeller, C. (2006). Two-dimensional indices of atmospheric blocking and their statistical relationship with winter climate patterns in the Euro-Atlantic region. *International Journal of Climatology*, *26*, 233–249.

Schiemann, R., Demory, M.-E., Shaffrey, L. C., Strachan, J., Vidale, P. L., Mizielinski, M. S., . . . Jung, T. (2017). The resolution sensitivity of Northern Hemisphere blocking in four 25-km atmospheric global circulation models. *Journal of Climate*, *30*(1), 337–358.

Shutts, G. (1983). The propagation of eddies in diffluent jetstreams: Eddy vorticity forcing of blocking flow fields. *Quarterly Journal of the Royal Meteorological Society*, *109*, 737–761.

Taylor, K. (2001). Summarizing multiple aspects of model performance in a single diagram. *Journal of Geophysical Research*, *106*(D7), 7183–7192.

Taylor, K., Stouffer, R., & Meehl, G. (2012). An overview of CMIP5 and the experiment design. *Bulletin of the American Meteorological Society*, *93*(4), 485–498.

Tibaldi, S., & Molteni, F. (1990). On the operational predictability of blocking. *Tellus, Series A*, *42*, 343–365.

Titchner, H. A., & Rayner, N. A. (2014). The Met Office Hadley Centre sea ice and sea surface temperature data set, version 2: 1. Sea ice concentrations. *Journal of Geophysical Research: Atmospheres*, *119*, 2864–2889. https://doi.org/10.1002/2013JD020316

Trenberth, K. E. (1986). An assessment of the impact of transient eddies on the zonal flow during a blocking episode using localized Eliassen-Palm flux diagnostics. *Journal of the Atmospheric Sciences*, *43*(19), 2070–2087.

Tyrlis, E., & Hoskins, B. (2008a). The morphology of northern hemisphere blocking. *Journal of Atmospheric Science*, *65*, 1653–1665.

Tyrlis, E., & Hoskins, B. (2008b). Aspects of a northern hemisphere atmospheric blocking climatology. *Journal of Atmospheric Science*, *65*, 1638–1652.

Valdes, P., & Hoskins, B. (1989). Linear stationary wave simulations of the time-mean climatological flow. *Journal of Atmospheric Sciences*, *46*, 2509–2527.

Vallis, G. (2006). *Atmospheric and oceanic fluid dynamics: Fundamentals and large-scale circulation*. Cambridge, UK: Cambridge University Press.

Vial, J., & Osborn, T. (2012). Assessment of atmosphere-ocean general circulation model simulations of winter northern hemisphere atmospheric blocking. *Climate Dynamics*, *39*(1), 95–112.